

Design, simulation, fabrication, packaging, and characterization of a MEMS-based mirror array for femtosecond pulse-shaping in phase and amplitude

Stefan M. Weber, Luigi Bonacina, Wilfried Noell, Denis Kiselev, Jérôme Extermann, Fabio Jutzi, Sébastien Lani, Ondrej Nenadl, Jean-Pierre Wolf, and Nico F. de Rooij

Citation: [Review of Scientific Instruments](#) **82**, 075106 (2011); doi: 10.1063/1.3606440

View online: <http://dx.doi.org/10.1063/1.3606440>

View Table of Contents: <http://scitation.aip.org/content/aip/journal/rsi/82/7?ver=pdfcov>

Published by the [AIP Publishing](#)



New, Easy-to-Mount
FLIR A6700sc Camera

When you need Science-Grade IR in Tight Spaces

FLIR

Get Datasheet ▶

The advertisement features a dark blue background with a glowing orange and yellow circuit board pattern. A black FLIR A6700sc camera is shown in the center, with its lens and the FLIR logo clearly visible. The text is arranged in a clean, professional layout, with the product name and tagline on the left, the FLIR logo on the right, and a call-to-action button at the bottom right.

Design, simulation, fabrication, packaging, and characterization of a MEMS-based mirror array for femtosecond pulse-shaping in phase and amplitude

Stefan M. Weber,^{1,a)} Luigi Bonacina,^{1,b)} Wilfried Noell,^{2,c)} Denis Kiselev,¹ Jérôme Extermann,¹ Fabio Jutzi,² Sébastien Lani,² Ondrej Nenadl,¹ Jean-Pierre Wolf,¹ and Nico F. de Rooij²

¹GAP-Biophotonics, Université de Genève, 20 rue de l'Ecole de Médecine, 1211 Genève 4, Switzerland

²EPFL/STI/IMT-NE/SAMLAB, Rue Jaquet-Droz 1, 2002 Neuchâtel, Switzerland

(Received 12 April 2011; accepted 8 June 2011; published online 12 July 2011)

We present an in-detail description of the design, simulation, fabrication, and packaging of a linear micromirror array specifically designed for temporal pulse shaping of ultrashort laser pulses. The innovative features of this device include a novel comb-drive actuator allowing both piston and tilt motion for phase- and amplitude-shaping, and an X-shaped laterally reinforced spring preventing lateral snap-in while providing high flexibility for both degrees of freedom. © 2011 American Institute of Physics. [doi:10.1063/1.3606440]

I. INTRODUCTION

Among the large and growing variety of applications based on Optical MEMS technologies (display devices,¹ adaptive optics,² waveguides,³ switches,⁴ spatial light modulators,^{5,6} etc.), a relatively new one is the temporal pulse shaping of ultrashort light pulses.⁷ Considering the time-scales involved in this process (femtoseconds to picoseconds), the shaping operation is realized in the frequency rather than in the time-domain by introducing arbitrary phase-shifts and/or amplitude modulations on the pulse individual frequency components.⁷ Presently, there exists quite a variety of shaping devices, whose operation principle is alternatively based on acousto-optic,⁸ electro-optic,^{9,10} or nematic liquid crystals,¹¹ the last ones being by far the most popular. These approaches, however, suffer from some limitations in terms of spectral flexibility, energy through-put, damage threshold, and speed. Most of these constraints are inherent to the transmissive nature of these devices. To circumvent them, Hacker *et al.*¹² in a pioneering work demonstrated the use of a 2D MEMS reflective device¹³ for temporal phase-shaping in the near UV opening the way to a series of further characterizations and experiments essentially focused on the possibility provided by this approach of accessing deeper UV spectral regions.^{14–16}

In this contribution, we present an in-depth review of a micromirror array specifically developed for femtosecond pulse shaping, incorporating the main requirements dictated by this application: broadband reflectivity, high duty cycle, low diffraction losses, large strokes, and low power densities. Another device from the same fabrication run which was capable of piston modulation only was already introduced and

successfully implemented in a femtosecond phase-sensitive experiment.¹⁷ Here, we present a more complex MEMS chip, capable of modulating both the amplitude and phase of ultrashort laser pulses by simultaneous piston and tilt mirror motion.

In the following we describe the design, simulation, fabrication, packaging, and characterization of the new MEMS chip, while another recent publication¹⁸ is dedicated to the in depth presentation and discussion of the spectral and temporal shaping results obtained with it.

II. OPERATION PRINCIPLE

As sketched in Fig. 1(a), the different spectral components within the input pulse bandwidth, are first angularly dispersed by a diffraction grating. A cylindrical lens at the focal distance f from the grating is then used for collimating the diffracted beam and focusing each spectral component onto the Fourier plane, which corresponds to the position of the reflective MEMS surface. When the mirrors are not actuated, the setup acts as a zero-dispersion $4-f$ compressor: the back reflected spectral components recombined after the second passage on the grating, interfere to produce an output pulse spectrally and temporally identical to the input one. When the shaper mirrors are offset from the Fourier plane (b), an arbitrary phase-pattern (ϕ) is imposed on the output beam through the relation $\Delta\phi = \frac{4\pi}{\lambda} \Delta z$, while the initial spectral amplitude is preserved. For instance, a parabolic phase function induces a temporal chirp on the outgoing beam. If some mirrors are tilted by a fixed angle around an axis perpendicular to the dispersion plane (c), two separate parallel beams emerge from the setup: one made up by the spectral components associated to the deflected (D) mirrors, and one by the complementary ones, reflected by the undeflected (U) mirror elements. Phase modulations can be independently added to these two beams by simultaneously translating and tilting the mirrors (d).

^{a)}Present address: Jenoptik Optical Systems GmbH, Business Unit Microoptics, Goeschwitzer Strasse 25, 07745 Jena, Germany.

^{b)}Electronic mail: luigi.bonacina@unige.ch.

^{c)}Electronic mail: wilfried.noell@epfl.ch.

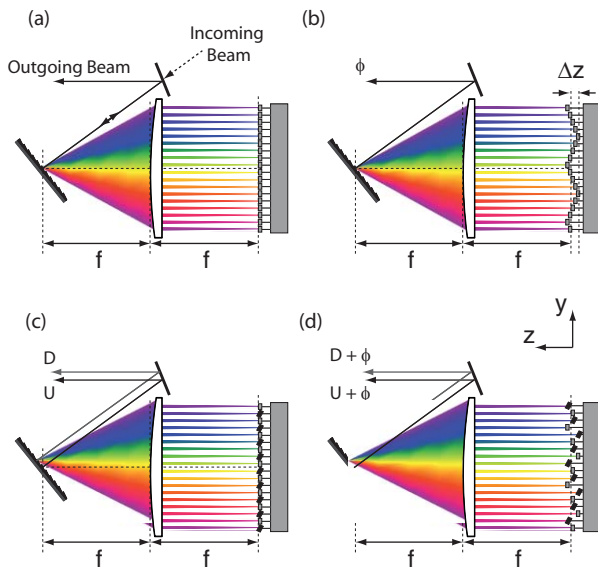


FIG. 1. (Color online) Principle of reflective femtosecond pulse shaping. (a) Pulse shaper with a flat phase and amplitude mask. (b) Piston actuation for phase-only shaping (ϕ), as in Ref. 17. (c) Tilt only actuation for binary amplitude modulation. (d) Simultaneous phase- and binary-amplitude-modulation, as in Ref. 18.

III. DESIGN CONCEPT

Table I summarizes the essential geometrical parameters of the design. Based on our previous experience with reflective MEMS devices for temporal pulse-shaping,¹⁵ we opted for a 1D array, preferable to minimize inter-mirror gaps and diffraction losses. Moreover, we choose to implement high aspect-ratio mirrors ($160\ \mu\text{m} \times 1000\ \mu\text{m}$), better matching the elongated focal spot of cylindrical optical elements, typically employed in zero-dispersion $4f$ arrangements. This geometry, i.e., using cylindrical instead of spherical mirror, additionally helps decreasing the laser power density on the reflective surface. A single mirror element with actuators is shown in Fig. 2, it features a symmetric geometry and actuation with the high-aspect ratio mirror (e) located in the center being clamped from both sides. The two types of actuators are tilt (c) and piston (d), connected via a height adapter (b) to the X-shaped springs (a) lying at the outer edges. Both degrees of freedom are enacted using a single spring: vertical comb drives^{19,20} are used in a symmetric way for out-of-plane piston movement and in an asymmetric manner for enacting the torque for tilting.

Obtaining a sufficient torque to rotate the mirror requires a large number of comb fingers for a given mirror pitch. This results in a very long lever arm, increasing dramatically the

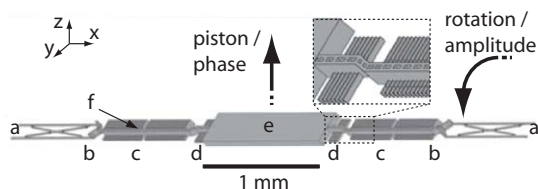


FIG. 2. Geometry of a single mirror element: X-shaped springs (a), triangular height adapter (b), tilt (c) and piston (d) actuators, high aspect-ratio mirror (e), and main bar (f).

TABLE I. Summary of the geometric properties of the device.

Description	Values
Number of mirrors	100
Mirrors used for this publication	26
Dimensions	
Mirror size	$160 \times 1000\ \mu\text{m}^2$
Mirror pitch	$163\ \mu\text{m}$
Mirror gap	$3\ \mu\text{m}$
Mirror height (device layer thickness)	$35\ \mu\text{m}$
Fill factor (in-plane)	98.2%
Chip dimensions	$7570 \times 17553\ \mu\text{m}^2$
Oxide layer thickness	$2\ \mu\text{m}$
Handle layer thickness	$350\ \mu\text{m}$
Delay mask process lower level height	$11\ \mu\text{m}$
Backside vertical slits (mirror release)	$300 \times 60\ \mu\text{m}^2$
Main bar release holes	$20 \times 6\ \mu\text{m}^2$
X-beam diameters	
Outer straight bar	$5\ \mu\text{m}$
X	$4\ \mu\text{m}$
Length	$700\ \mu\text{m}$
Height	$11\ \mu\text{m}$
Actuation	
Target piston stroke	$1\ \mu\text{m}$
Piston stroke measured, at 100 V	$2.5\ \mu\text{m}$
Target tilt angle (optical)	1°
Tilt angle measured at 100 V	0.67°
Piston comb pairs each side	7
Tilt comb pairs each side	57
Surface deformation	
Single mirror, R_z , at 80 V	$16\ \text{nm}$
Single mirror, R_a , at 80 V	$2.5\ \text{nm}$
Packaging	
Bond pad pitch	$81.5\ \mu\text{m}$
Bond pad size	$300 \times 130\ \mu\text{m}^2$
Gold wirebond lengths (projection)	$2.4\text{--}3.8\ \text{mm}$
Wirebonds to PCB each side	201
Chip-internal wirebonds	100
Total wirebonds	502
Electronics	
Interconnect PCB (ICP) size	$46 \times 46 \times 0.8\ \text{mm}^3$
ICP material	FR-4
ICP lines and spaces	$50\ \mu\text{m}$
ICP microvia diameter	$180\ \mu\text{m}$
ICP through-hole diameter	$200\ \mu\text{m}$

risk for premature lateral pull-in.²¹ To avoid this effect, we developed the laterally reinforced spring labeled (a) in Fig. 2, which combines flexibility in both piston and tilt while still being stiff in respect to an in-plane force. In fact, a V- or H-shaped spring^{22–26} alone would not have provided the requirements on lateral stability, and therefore two thin beams were added to an X-shaped spring. The beam comprises the X-part ($4\ \mu\text{m}$ diameter) and two outer bars ($5\ \mu\text{m}$ diameter). All dimensions, including the overall length ($700\ \mu\text{m}$) and height ($11\ \mu\text{m}$) were optimized to produce a viable compromise between the stability and the specified angle and piston motions. The springs are connected to the main bar (f) via a triangular structure (b). To further reduce optical diffraction, no mirror release holes were designated, the mirrors were instead released using backside openings slits.

The application requirements impose that the device presents a flat ($\lambda_0/20$, λ_0 being the central wavelength of the pulse spectrum) uninterrupted surface and large strokes ($\geq \lambda_0/2$) allowing $\geq 2\pi$ phase-modulation in a reflective design. Concerning the tilt amplitude, the deflection angle necessary to reject specific spectral components was determined to be at least 1° , corresponding to 2° optical deflection.

IV. SIMULATIONS

We performed a series of finite elements simulations using the COMSOL Multiphysics software environment. Due to the complexity of the system and the large number of comb fingers involved, a full electro-mechanically coupled analysis was omitted. Instead, first a mechanical model was composed as complete as possible including the comb fingers (Sec. IV A). Second, a limited but still meaningful electrostatic (ES) model was developed (Sec. IV B). Finally, the resulting torques and forces derived from this partial ES-model were transferred to the complete mechanical model, for a coupled simulation (Sec. IV C).

A. Mechanical model – X-shaped springs

As one can see in Fig. 3, which summarizes the results of the mechanical simulations, the predominant fraction of the structural deformation upon actuation goes into the X-shaped beam. The mirror deforms by 11 nm peak-to-valley (PTV), when displaced by $z = 2.76 \mu\text{m}$, corresponding to 100 V applied voltage. The mechanical stress in the X-shaped beam under piston and tilt actuation is detailed in Fig. 4. For the piston case, the largest stress is located at the outer ends of the X-beam, at the straight bars, while for rotation, it is more distributed and also present at the central intersection.

An alternative procedure for analyzing the stability is calculating the stored mechanical energy and energy densities in the actuated states. This was derived by integrating the Mises stress over the total volume of the respective element (mirror, X-beam, etc.). The inset of Fig. 3 summarizes the results of this procedure in the case of (1) two different piston actuations, (2) simultaneous piston and tilt movement,

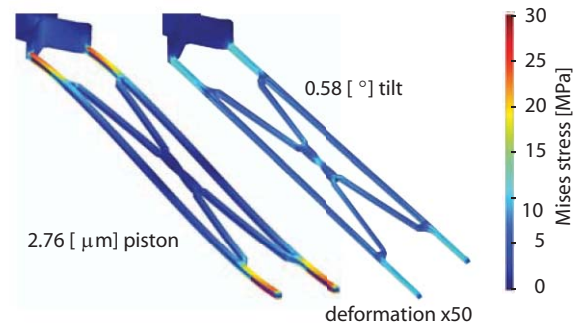


FIG. 4. (Color online) Comparison of the stress in the X-beam for: 2.76 μm piston actuation (left) and 0.58° tilt (right). The deformation is multiplied by a factor of 50 for easier inspection.

(3) tilt-only, and (4) when a lateral force is applied. Again, one can appreciate how the X-beams act for improving stability by absorbing a large amount of energy compared to their volume, particularly in the case of a lateral deformation, while the energy-density stored in the mirrors appears always relatively small, resulting in low deformations.

The resonance frequencies are listed in Table II. The lowest mode at 3.11 kHz is associated with the piston motion, an undesired lateral mode comes next at 7.83 kHz. The fundamental tilt mode comes in at 13.97 kHz. At much higher frequencies, one can also observe more complex motion patterns, for example, a butterfly-mode of the X-beam at 153 kHz, defined by the opposite oscillations of the crossed beams and the outer bars. On the basis of this frequency analysis, one can expect that the device is capable of operating at the typical 1 kHz repetition rate of an amplified Ti:sapphire laser system, providing a different shaping pattern at each laser shot.

B. Electrostatical model—asymmetrical comb drive

To achieve the required torque, a novel asymmetrical vertical comb drive was developed. The operation concept

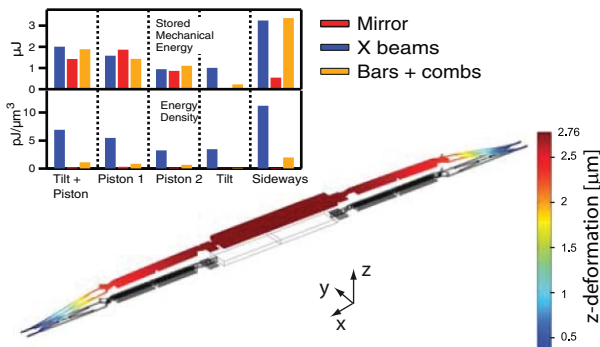


FIG. 3. (Color online) Mechanical model. The deformation, when the mirror element is actuated by $2.76 \mu\text{m}$ (100 V) in piston mode, is 11 nm PTV. If the analysis is restricted to the central $400 \mu\text{m}$ of the mirror, this value drops down below 2 nm. Inset: stored mechanical energy and energy density of the mirror components for various different actuation states.

TABLE II. Resonance frequencies of the calculated mechanical modes.

Mechanical mode	Resonance frequency [kHz]	Harmonics number	Description
1	3.11	1	Ppiston
2	7.83	1	Lateral
3	10.43	2	Piston
4	13.97	1	Tilt
5	23.55	2	Lateral
6	38.59	3	Piston
7	60.94	4	Piston
8	63.49	3	Lateral
9	73.23	4	Lateral
10	128.37	5	X-beams, piston symmetrical
11	135.18	5	X-beams, piston asymmetrical
12	152.69	1	X-beam butterfly

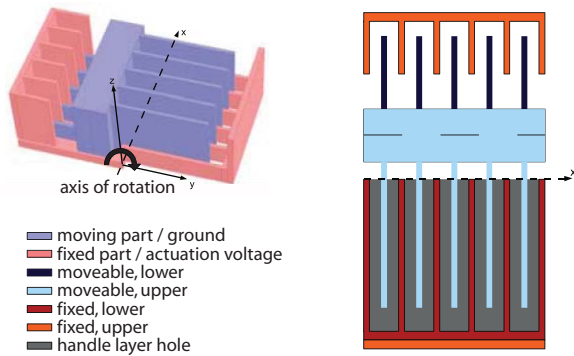


FIG. 5. (Color online) 3D model of an asymmetric comb drive (3D and top view).

is sketched in Fig. 5: when voltage is applied on both the right and left outer combs, the actuator performs a clockwise rotation. To estimate the total torque exerted on the moving part, we set up an electrostatic finite element method (FEM) model limited to five comb pairs, this partial simulation allowed keeping a reasonable model accuracy without introducing excessive computational complexity. The calculated torque from this reduced model was then scaled up to the actual dimensions. These simulations have permitted to optimize the geometry of this component for simultaneously providing a large torque around the x -axis while minimizing lateral and out-of-plane contributions, along y - and z -axis. A second goal of the numerical optimization procedure was to obtain an equal torque contribution from the left (lower comb level) and right (upper comb level) side. In fact, an unbalanced asymmetrical comb drive would have been more susceptible to premature pull-in. The latter has the tendency to appear when the oppositely charged surfaces of comb and fixed parts are at different heights. To compensate for this effect, the distance of the upper level combs to the sidewalls was increased to $8\ \mu\text{m}$, minimizing the rotation around the z -axis.

During the optimization runs, the geometry shown in Fig. 5 was varied until a sufficiently large ratio contrast was obtained. In particular, an indication given by the simulations was to remove the substrate below the comb fingers, so that the upper level combs achieve a torque comparable to those on the lower level. Furthermore, the optimization procedure helped realizing that the comb overlap had to be increased for the upper combs by offsetting the main bar by $15\ \mu\text{m}$ from the rotational axis. From this FEM analysis, we determined that the largest torque contributions originated from the two distinct comb edges: (1) from the outer, upper edge of the lower comb fingers and (2) from the outer, bottom edge of the higher comb fingers. Therefore, we considered it sufficient for the following electromechanical simulations, to apply the resulting torques only at the comb edges of the mechanical model. We also observed that the x -torque (contributing to tilt) slowly decreases for higher tilt angles, but we ensured that the contributions along y and z always remain negligible.

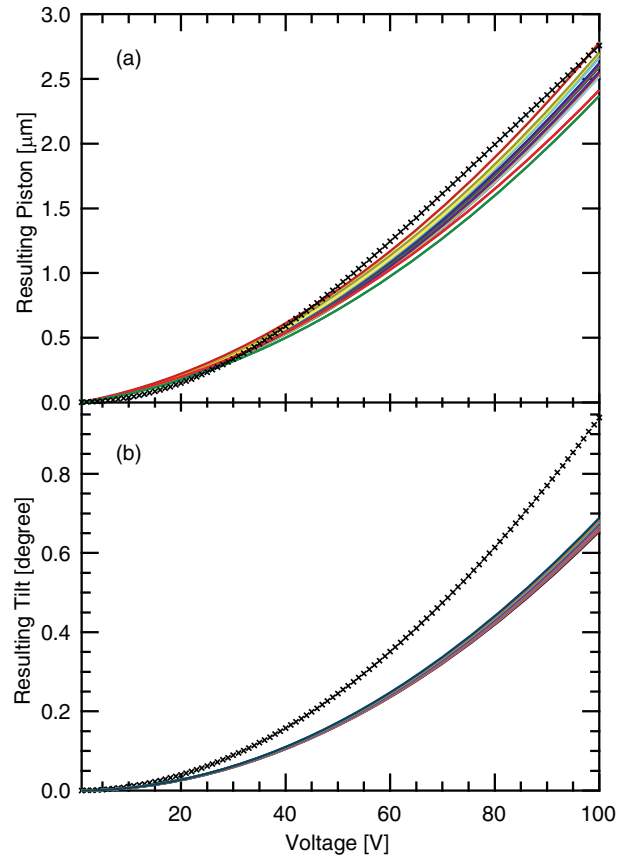


FIG. 6. (Color online) (a) Voltage-piston relation and (b) voltage-tilt relation. Crosses: results from the simulations. Colored lines: values measured for different mirrors of the fabricated device.

C. Combined electrostatic/mechanical analysis

The force equilibrium between mechanical force and the electrostatic force/torque provides an estimation for the achievable piston and tilt for any actuation voltage. In Fig. 6, the crosses representing the calculated voltage-to-piston (a) and the voltage-to-tilt relation (b), are directly compared with the experimental responses measured on several device mirrors (multicolored lines). For the piston case (Fig. 6(a)), one can appreciate the good agreement between the experimental and the numerical traces. Moreover, we remark that the spread among the response of the different mirrors remains rather small. On the other hand, for the tilt case (Fig. 6(b)), the agreement with simulation is clearly less pronounced. We, therefore, considered necessary to directly measure the actual deformation of the X-beam structure when actuated by $70\ \text{V}$, as the latter is the most flexible and critical component. The deformation is visualized in the white-light interferometric measurement displayed in Fig. 7. The inspection ensures that the anchored parts are located at the same height and the rest of the structure twists under the applied torque, as expected.

V. FABRICATION

The device was fabricated using SOI (silicon-on-insulator) wafers of $35\ \mu\text{m}$ device-, $2\ \mu\text{m}$ oxide- and $350\ \mu\text{m}$ thick handle-layer. Using a delayed-mask process, two

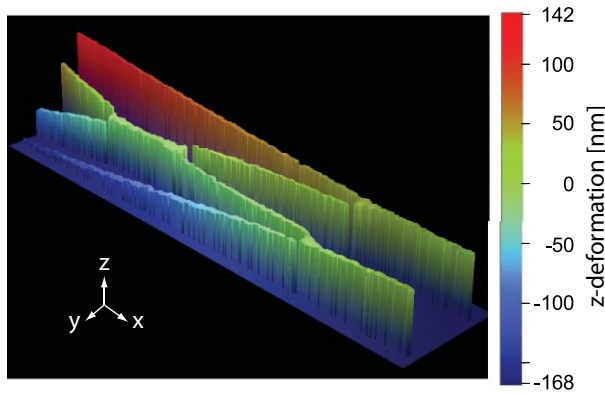


FIG. 7. (Color online) White-light interferometric measurement of the deformed X-beam (phase shifting interferometry mode) for an actuation voltage of 70 V.

different height levels were fabricated by a self-aligned DRIE (deep-reactive-ion etching). No release holes were required for the mirrors, as we etched long release openings from the backside into the handle layer. This procedure is particularly important, as having an uninterrupted mirror surface limits beam diffraction, a severe drawback for the optical applications envisaged that we also pointed out in previous works.¹⁵ After the DRIE process, a thermal oxidation procedure was applied for eliminating silicon residues. The devices were released by HF vapor-phase etching prior to metalization. We found that a 10/300 nm Ti/Al metal coating provides an acceptable compromise between reflectivity and adhesion for the gold wirebonding. The metal evaporation was performed without a shadow mask, covering the entire chip surface. The SEM image in Fig. 8 contains a detailed image of a symmetric comb drive.

VI. PACKAGING

We developed a packaging system consisting of an interconnect printed circuit board (PCB), fine-pitch gold wirebonding, and a socket with spring loaded contacts. The

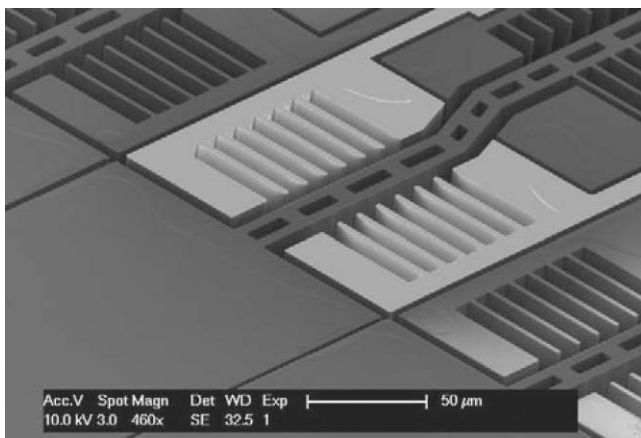


FIG. 8. Detail view of the symmetric piston comb drive (cross-section from a cut device).

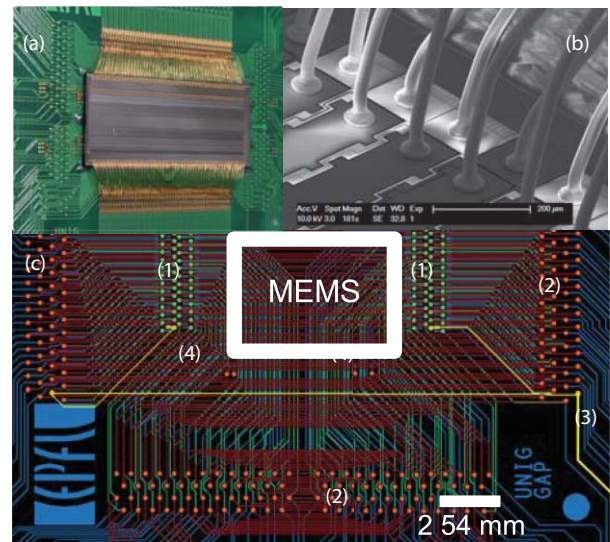


FIG. 9. (Color online) (a) Actual picture of the PCB. (b) Close-up of the outgoing wirebonds. (c) Schematic view of the four-level PCB (partial view) with microvias (1) and through-holes (2). The chip is connected by wirebonds across zone 4 onto the gold bond pads which are accompanied by microvias. The pads are arranged in rows of four times 50 pads on each side. Two connectors on each side are cross-connected inside the PCB due to the symmetrical properties of the device (horizontal line highlighted) connecting two bondpads from the left and right side to the backside, larger contact gold pad (3).

socket is inserted in a home-made electronics based on eight AD5535 high-voltage D/A converters with 204 independent 14-bit resolution high-voltage channels. The chip itself is glued on the PCB board with an epoxy glue.

A. Interconnect PCB board

The material chosen for the PCB was FR-4, high-density routing with 50 μm lines and spaces, 180 μm diameter microvias, and 200 μm diameter through-holes. The design requirements were the limit of commercially available technology for small-scale production. The final PCB board ((46 × 46 × 0.8) mm³) is shown in Fig. 9(a). The MEMS chip is glued in the center. Panel (c) displays a part of the design drawing of the four levels needed to cross-connect all 400 bond pads, i.e., two connections on each element side plus one mandatory ground line. The routing connects symmetrical bondpads to a 18 × 18 pin grid array supplying the 200 independent voltage channels.

B. Wirebonding

The wirebonding was performed using a fine-pitch, ball-wedge gold wirebonder employing 35 μm diameter gold wires. Gold wirebonding was chosen in order to employ flexible, multilevel, and few-millimeter long wirebonds, but to also have the possibility to add close-distance interconnects on the chip itself to ground the mirrors via a hole in the device layer. This procedure allows eliminating the need for a fifth wirebonding level.

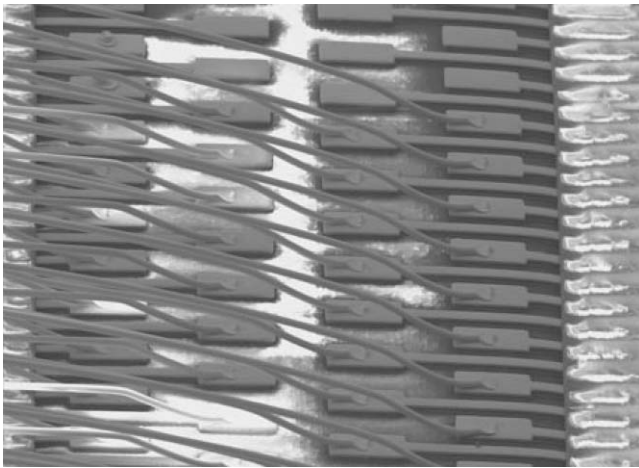


FIG. 10. Detail view of the four level wirebonding using 35 μm diameter gold wires.

The connections density of the four-level wirebonding can be fully appreciated from Fig. 10. Two starting points for piston and tilt from each side of each mirror are connected to four wirebond pads rows as they have a larger pitch.

VII. CHARACTERIZATION, CALIBRATION, AND DECOUPLING

The optical characterization was performed with a Veeco/Wyko NT1100 DMEMS optical profiler. From the first run of fabricated devices, the device with the highest yield of working mirrors unfortunately had an overall curvature too large to be self-compensated by the piston movement (as for Ref. 17). Therefore, for the optical experiments, only a limited region with local curvature within the compensation range was considered.

The device calibration was performed on a mirror-by-mirror basis by measuring the position and tilt of each mirror element as a function of the voltage applied to the piston and tilt actuators. An exemplary surface resulting from this treatment is plotted in Fig. 11. A rapid inspection of the curves indicates the presence of a coupling among the two degrees of freedom, affecting principally the piston movement: the mirror is pulled downwards, if a tilt voltage is applied. Although a considerable effort was undertaken to reduce such a downwards torque component, the effect could not be fully avoided. The dependency of the tilt angle on the piston voltage, however, remains very small.

To decouple piston and tilt movement for independently addressing each mirror motion, we performed a surface fit of the data to provide an analytical description of every mirror response (z, θ) as a function of the voltages U_p, U_t applied to the respective actuators. We determined that 7 is the minimal number of parameters for a proper fitting the piston response, z , by the following expression:

$$z(U_t, U_p) = p_{00} + p_{01}U_p + p_{20}U_t^2 + p_{02}U_p^2 + p_{30}U_t^3 + p_{21}U_t^2U_p + p_{12}U_tU_p^2, \quad (1)$$

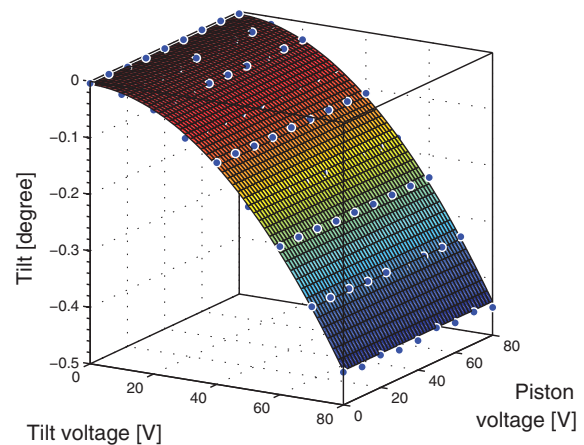
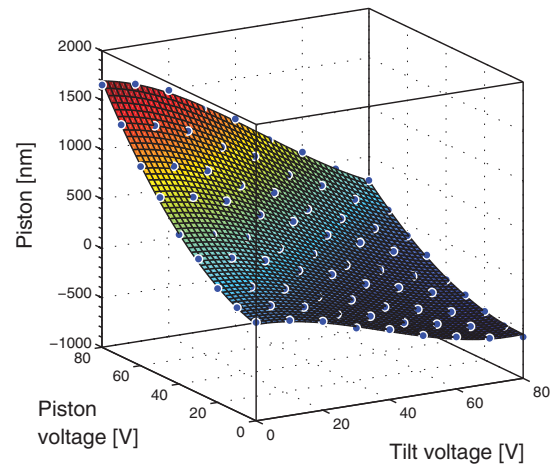


FIG. 11. (Color online) Measured piston (a) and tilt (b) actuation as a function of the applied voltages for an exemplary mirror. Dots: experimental data points; segmented surfaces: results of the analytical fitting functions given in Eqs. (1) and (2).

while the tilt θ could be reasonably fitted by a simpler expression

$$\theta(U_t, U_p) = t_{00} + t_{20}U_t^2 + p_{11}U_tU_p, \quad (2)$$

where the coupling coefficient p_{11} can be also neglected. The coefficients t_{00} and p_{00} correspond to the residual offset at $U_p, U_t = 0$ V. The parameters p_{20}, p_{21} , etc. indicate the coupling terms.

Aside from the piston-tilt coupling, we also observed a minor tilt along the y -axis, up to $\pm 0.009^\circ$. Although this value is small, the effect of such a tilt along a one-millimeter long mirror, can amount to the height differences up to ± 150 nm. The reason for this could be residual stress from the SOI wafer, but also the soft material of the interconnect PCB and partially packaging. This effect drastically reduces the otherwise excellent surface quality: the roughness of the single mirrors (including the Ti/Al metallization) remains in fact below 16 nm PTV. A slight increase of the mirror deformation for the piston actuation compared to tilt (both at 80 V) was also observed, in agreement with our simulation.

As an example of device addressing, in Fig. 12 we provide an exemplary interferometric image of five consecutive mirrors actuated in piston and tilt by an arbitrary pattern. The voltages applied are listed in Table III.

TABLE III. Voltages applied to generate the pattern of Fig. 12 and measured piston and tilt actuation.

Mirror number	Piston measured		Tilt measured	
	U_p [V]	[μm]	U_t [V]	[degree]
96	80	0	60	0.42
97	60	1.15	0	<0.001
98	80	0	60	0.42
99	0	0	0	<0.001
100	80	0.2	80	0.46

VIII. OPTICAL MEASUREMENTS

A. Damage threshold determination

In order to establish safe working conditions for the MEMS device, the chip was tested using a variety of damage threshold detection techniques. The measurements were based on the frequency tripled output (266 nm) of an amplified Ti:sapphire system working at a 1 kHz repetition rate with a maximal pulse energy of 20 μJ . The UV pulse duration was ~ 160 fs as determined by a down conversion cross frequency resolved optical gating (FROG) measurement in a beta-barium borate (BBO) crystal. During the exposure to the UV beam, we performed a series of reflectivity tests, monitoring the reflected intensity and the beam profile of a probe HeNe laser beam incident on the same spot of the UV. Alternatively, we carefully characterized the irradiated chip areas after long time exposures (>40 min) by optical stereo-microscopy, SEM, and white light interferometry. For the unfocused beam (1 mm diameter at FWHM), we report no effects on reflectivity nor the presence of damaged spots on the surface. Moreover, the comparison among interferometric measurements performed before and after the exposure to the fs laser, indicate no bending or any other light-induced surface alterations of the chip. By focusing the beam onto the device (focal spot 130 μm diameter at FWHM), we could determine the damage threshold for short-pulse operation around $5 \times 10^8 \text{ W/cm}^2$. Considering the difficulty to compare this value, determined with ultrashort fs laser pulse, with those more often reported for continuous wave or nanosecond pulsed laser and with the aim to provide a more user-oriented information, we provide a calculation based on realistic experimental conditions. We consider a 30 μJ deep UV

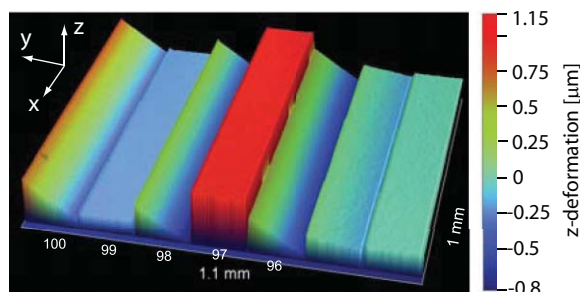


FIG. 12. (Color online) Interferometric image corresponding to an arbitrary five mirrors independent piston and tilt actuation. The corresponding piston and tilt voltages are listed in Table III.

(266 nm) pulse with a spectral bandwidth of 2 nm FWHM (52 fs Fourier limited duration), spatial beam of diameter 1 mm FWHM, entering into a pulse-shaper based on a 3600 grooves/mm grating, and 30 cm focal length collimating optics (cylindrical mirror or lens). In the calculation, we suppose that the pulse duration of each individual spectral component resolved by the system at the Fourier plane is 1.3 ps (0.08 nm). With these figures, the peak intensity onto the central pixel of the device (irradiated by $\sim 4.5\%$ of the total spectral intensity) corresponds to $\sim 3 \times 10^8 \text{ W/cm}^2$, and it is therefore safe for the device. With our shaper setup, we measured an overall throughput of 15%, which, after correction for the measured grating efficiency and taking into account the lens reflection, yields a value of $\sim 65\%$ efficiency of the chip at 266 nm. Losses are due to the Al coating reflectivity (85% at this wavelength) and pixelization (fill factor and diffraction). For comparison, the damage threshold of the UV dazzler, at present the unique pulse-shaper device working in the deep UV commercially available, is 10^8 W/cm^2 , and its throughput is modulated by two-photon absorption in the potassium dihydrogen phosphate (KDP) crystal: 40% for a 2.5 μJ input pulse and 20% for a tenfold more intense pulse.^{27,28}

B. Pulse shaping

Figure 13 presents the device assembled and ready for being implemented in an optical setup. The driving electronics is housed inside the aluminum box (165 mm \times 250 mm) that can be directly clamped to an optical table and provides three adjustment screws. An ethernet or USB connection allows to program the desired mask pattern on the device.

Experimental demonstrations and detailed discussions about phase-only and phase-and-amplitude pulse shaping can be found in Refs. 17 and 18, respectively. Here, we present an additional example of the capabilities of the device. Using a setup identical to Ref. 17 we illustrate in Fig. 14 the

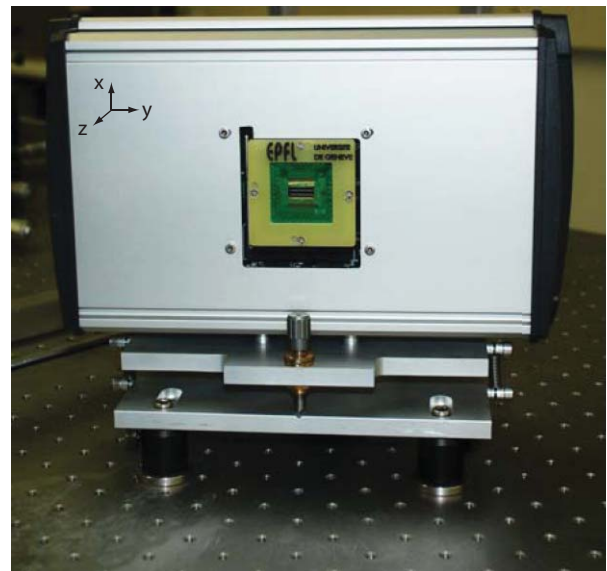


FIG. 13. (Color online) MEMS chip and driving electronics assembled in a dedicated opto-mechanical container.

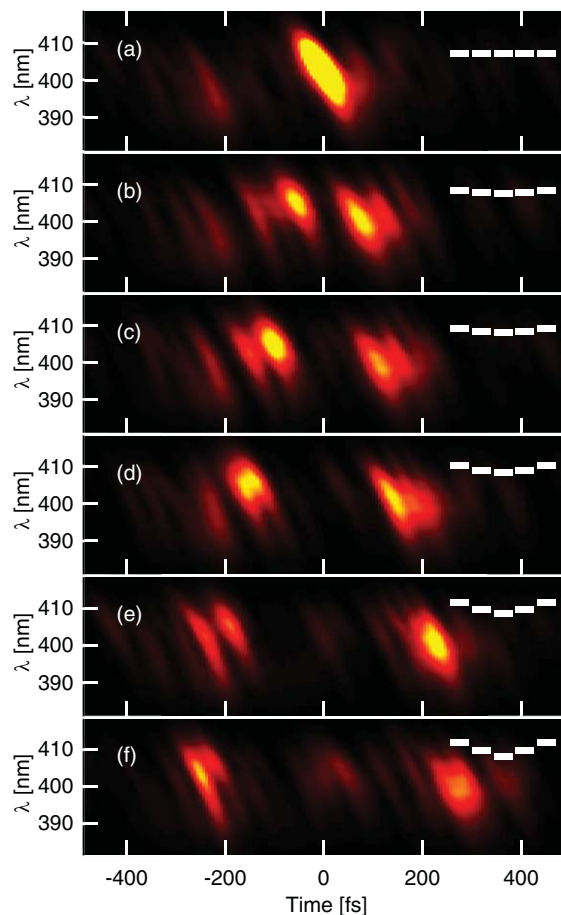


FIG. 14. (Color online) Cross-FROG measurements of the two sub-pulses at increasing delays generated by phase-only shaping. The intensity scale is kept identical for all traces. The symbolic mirrors representation in the top right corners give a suggestive and simplified indication of the phase-masks applied on the chip.

generation of a pair of two sub-pulses associated to the red and blue spectral components of the input pulse. An analogous pulse-shape has been proposed for time-domain single-beam coherent anti-Stokes Raman spectroscopy, coherent anti-Stokes Raman spectroscopy (CARS).²⁹ By applying a linear phase mask in the form of $\phi(\omega) = |\phi(\omega - \omega_0)|$ where ω_0 is the central frequency of the laser, we modulate the temporal distribution of the pulse intensity: the delay τ between the two sub-pulses corresponds to $\tau = \frac{d\phi}{d\omega}$. The characterization of the shaped pulses is realized by a cross frequency-resolved-optical-gating³⁰ using an external short reference pulse as a gate. The tilting present in all traces with respect to the wavelength axis indicates an uncompensated chirp of the input pulse. Starting from $\tau = 0$ fs in Fig. 14(a), we increase the delay τ by steps of 50 fs, up to $\tau = 250$ fs (Figs. 14(b)–(e)). One can note the signature of at least one nonworking mirror by the presence of unmodulated frequencies in the temporal domain, for example at -200 fs.

IX. CONCLUSIONS AND OUTLOOK

In this technical contribution, we have thoroughly described the design, simulation, fabrication, packaging, and characterization of our first demonstrator of a piston and

tilt micromirror array specifically developed for femtosecond laser pulse shaping. Although we have pointed out a number of issues which have still to be solved in the next fabrication iterations, the measurements performed under standard experimental conditions in a femtosecond laser laboratory reported here and in two accompanying papers^{17,18} testify the potential and versatility of this new device.

ACKNOWLEDGMENTS

We gratefully acknowledge Severin Waldis for the first design, N. Onda and J. Langer (Altatec AG) for the wirebonding development, the Div. C of the CSEM (CH-Neuchâtel), Photochemie AG for the PCB fabrication, E-Tec SA for the interconnect solution, and the Swiss National Science Foundation/ NCCR Quantum Photonics QP8 and NCCR MUST for financial support.

- ¹D. Dudley, W. Duncan, and J. Slaughter, *Proc. SPIE* **4985**, 14 (2003).
- ²M. A. Helmbrecht, U. Srinivasan, C. Rembe, R. T. Howe, and R. S. Muller, *Transducers '01: Eurosensors XV, Digest of Technical Papers*, Vols. 1 and 2, pp. 1290–1293 (2001).
- ³E. Ollier, *IEEE J. Sel. Top Quantum Electron.* **8**(1), 155 (2002).
- ⁴T. W. Yeow, K. L. E. Law, and A. Goldenberg, *IEEE Commun. Mag.* **39**(11), 158 (2001).
- ⁵S. Yamashita, M. Mita, H. Fujita, R. Hirade, T. Yamamoto, M. Kawai, and M. Yano, *J. Microelectromech. Syst.* **20**(1), 270 (2011).
- ⁶S. Yamashita, M. Mita, H. Fujita, T. Yamamoto, M. Kawai, and M. Yano, *J. Microelectromech. Syst.* **20**(1), 279 (2011).
- ⁷A. M. Weiner, *Rev. Sci. Instrum.* **71**(5), 1929 (2000).
- ⁸P. Tournois, *Opt. Commun.* **140**(4–6), 245 (1997).
- ⁹C. W. Hillegas, J. X. Tull, D. Goswami, D. Strickland, and W. S. Warren, *Opt. Lett.* **19**(10), 737 (1994).
- ¹⁰M. Roth, M. Mehendale, A. Bartelt, and H. Rabitz, *Appl. Phys. B: Lasers Opt.* **80**(4–5), 441 (2005).
- ¹¹A. M. Weiner, J. P. Heritage, and E. M. Kirschner, *J. Opt. Soc. Am. B* **5**(8), 1563 (1988).
- ¹²M. Hacker, G. Stobrawa, R. Sauerbrey, T. Buckup, M. Motzkus, M. Wildenhain, and A. Gehner, *Appl. Phys. B: Lasers Opt.* **76**(6), 711 (2003).
- ¹³A. Gehner, W. Doleschal, A. Elgner, R. Kauert, D. Kunze, and M. Wildenhain, *Proceedings SPIE* **4561**, 265 (2001).
- ¹⁴R. Belikov, C. Antoine-Snowden, and O. Solgaard, 2003 IEEE/Leos Int. Conf. Optical Mems **180**, 24 (2003).
- ¹⁵A. Rondi, J. Extermann, L. Bonacina, S. M. Weber, and J. P. Wolf, *Appl. Phys. B: Lasers Opt.* **96**(4), 757 (2009).
- ¹⁶J. Mohring, T. Buckup, C. S. Lehmann, and M. Motzkus, *J. Opt. Soc. Am. B* **26**(8), 1538 (2009).
- ¹⁷S. M. Weber, J. Extermann, L. Bonacina, W. Noell, D. Kiselev, S. Waldis, N. F. de Rooij, and J. P. Wolf, *Opt. Lett.* **35**(18), 3102 (2010).
- ¹⁸J. Extermann, S. M. Weber, D. Kiselev, L. Bonacina, S. Lani, F. Jutzi, W. Noell, N. F. de Rooij, and J. P. Wolf, *Opt. Express* **19**(8), 7580 (2011).
- ¹⁹L. Y. Lin, J. L. Shen, S. S. Lee, G. D. Su, and M. C. Wu, *Mems 97*, IEEE Tenth Annual Int. Workshop on Micro Electro Mechanical Systems, pp. 43–48 (1997).
- ²⁰T. Overstolz, P. A. Clerc, M. T. Gale, H. P. Herzig, G. Niederer, W. Noell, J. Sochtig, H. Thiele, and N. F. de Rooij, *IEEE/Leos Int. Conf. Opt. Mems, Conf. Dig.* **211**, 81 (2002).
- ²¹S. Waldis, S. M. Weber, W. Noell, J. Extermann, D. Kiselev, L. Bonacina, J. P. Wolf, and N. F. de Rooij, *IEEE/Leos Int. Conf. Opt. Mems Nanophotonics* 39–40 (2008).
- ²²J. L. A. Yeh, C. Y. Hui, and N. C. Tien, *J. Microelectromech. Syst.* **9**(1), 126 (2000).
- ²³O. Tsuboi, Y. Mizuno, N. Koma, H. Soneda, H. Okuda, S. Ueda, I. Sawaki, and F. Yamagishi, *Fifteenth IEEE Int. Conf. Micro Electro Mech. Syst., Tech. Dig.* **737**, 532 (2002).
- ²⁴S. Ide, K. Mori, T. Akashi, Y. Sakai, T. Yamabana, Y. Ishii, O. Tsuboi, and M. Kawai, In *Eur. Conf. Optical Communication (ECOC)* (Rimini, Italy, 2003).

- ²⁵X. Y. Mi, H. Soneda, H. Okuda, O. Tsuboi, N. Kouma, Y. Mizuno, S. Ueda, and I. Sawaki, *J. Opt. A, Pure Appl. Opt.* **8**(7), S341 (2006).
- ²⁶C. Lee, *Microsyst. Technol. Micro Nanosyst. Inf. Storage Process. Syst.* **12**(8), 717 (2006).
- ²⁷S. Weber, M. Barthelemy, and B. Chatel, *Appl. Phys. B: Lasers Opt.* **98**(2–3), 323 (2010).
- ²⁸D. J. McCabe, D. R. Austin, A. Tajalli, S. Weber, I. A. Walmsley, and B. Chatel, *J. Opt. Soc. Am. B: Opt. Phys.* **28**(1), 58 (2011).
- ²⁹B. von Vacano and M. Motzkus, *Phys. Chem. Chem. Phys.* **10**(5), 681 (2008).
- ³⁰R. Trebino, K. W. DeLong, D. N. Fittinghoff, J. N. Sweetser, M. A. Krumbugel, B. A. Richman, and D. J. Kane, *Rev. Sci. Instrum.* **68**(9), 3277 (1997).